

## Supporting Information

### Portable NMR with Parallelism

Ka-Meng Lei<sup>†,‡</sup>, Dongwan Ha<sup>‡</sup>, Yi-Qiao Song<sup>§</sup>, Robert M. Westervelt<sup>†,||</sup>, Rui Martins<sup>†,⊥</sup>, Pui-In Mak<sup>\*,†</sup>, and Donhee Ham<sup>\*,‡</sup>

<sup>†</sup>State Key Laboratory of Analog and Mixed-Signal VLSI, University of Macau, Macau, China.

<sup>‡</sup>John A. Paulson School of Engineering and Applied Sciences, Harvard University, Cambridge, MA 02138.

<sup>§</sup>Schlumberger-Doll Research Center, Cambridge, MA 02139.

<sup>||</sup>Department of Physics, Harvard University, Cambridge, MA 02138.

<sup>⊥</sup>Instituto Superior Técnico, Universidade de Lisbon, Lisbon, Portugal.

\*E-mail – [pimak@um.edu.mo](mailto:pimak@um.edu.mo) and [donhee@seas.harvard.edu](mailto:donhee@seas.harvard.edu).

#### Table of Contents

Note 1: implementation of sample rotation .....	Page S-2
Note 2: NMR/MRI coils .....	Page S-3
Note 3: customized tube for two samples of different types .....	Page S-4
Note 4: NMR data processing .....	Page S-5
Note 5: magnetic-particle-based biomolecular sensing with parallelism.....	Page S-6
Note 6: design of the gradient coils for MRI system.....	Page S-7
Note 7: electronics for the gradient coils of MRI system .....	Page S-8
Fig. S1: block diagrams of the proposed NMR spectrometer and relaxometer with parallelism.....	Page S-9
Fig. S2: simulated magnetic-field pattern of the NMR coil .....	Page S-10
Fig. S3: the layout of the shim coils fabricated on PCB for 2 NMR samples .....	Page S-11
Fig. S4: time-interleaved 1D <sup>1</sup> H NMR spectroscopic experiment .....	Page S-12
Fig. S5: the gradient-coil for relaxometry .....	Page S-13
Fig. S6: measured diffusion-edited NMR relaxation data of skim milk.....	Page S-14
Fig. S7: relaxation rates measurement from avidin samples with the NMR relaxometer .....	Page S-15
Fig. S8: design and simulation of the MRI gradient-coils .....	Page S-16
Fig. S9: the hardware for the portable MRI .....	Page S-17
Fig. S10: the MRI experiment on the phantom .....	Page S-18
Fig. S11: original data for the high-throughput <i>T</i> <sub>2</sub> -screening with MRI .....	Page S-19
References .....	Page S-20



## Supplementary Notes

### **1. Implementation of sample rotation**

We use a SE10G brush DC motor from Minebea Mitsumi (Miyota, Japan). Its rotation speed is regulated by a motor driver BD6211F from Rohm Semiconductor (Kyoto, Japan). To transfer the torque from the motor to the PTFE tube, we make a gear train by printing two gears on a 1/8-inch thick acrylic sheet using a laser cutter Helix 75W from Epilog (Golden, CO) with the teeth ratio of 1:2 from the motor shaft to the PTFE tube. The motor and the magnet are placed on a 3D-printed holder.

## **2. NMR/MRI coils**

Each NMR coil for spectroscopy is a 5-turn solenoid (length: 0.8mm; ID: 1.8 mm) wound with 34 AWG enamel copper wire from Remington Ind. (Johnsburg, IL). Each NMR coil for relaxometry is the same construction except having 10 turns (length: 1.6 mm). The NMR coil for MRI uses the same wire but is a 6-turn solenoid (length: 1.0 mm; ID: 13 mm). They are all designed with COMSOL Multiphysics.

### **3. Customized tube for two samples of different types**

We first inject enough amount of UV adhesive glue into the center of the tube with a needle. The tube is then treated with UV light for 2 minutes to harden the glue that now functions as a spacer (Fig. 1b in the paper). After the samples are injected near the spacer into the tube with needles, both ends of the tube are injected with UV adhesive glue and treated with UV light to block the flow of the samples. Finally, a seal ring encloses the openings created by the needles to avoid leakage and also to prevent the infiltration of air into the samples, which could affect the magnetic susceptibilities of the samples and result in poor NMR spectra.

#### 4. NMR data processing

The NMR signals acquired by the silicon chip are digitized with 14-bit ADCs (LTC1407A, Analog Devices (Norwood, MA)) and collected by the microcontroller. We calibrate the temperature-dependent  $B_0$  fluctuation of the Halbach magnet [-400 ppm/K<sup>1</sup>] using the method of Ref. 2. The  $f_1$ -noises of the COSY spectrum are removed by utilizing the symmetric property of the COSY spectrum with respect to the diagonal line<sup>3</sup>. The  $D$ - $T_2$  maps and  $T_1$ - $T_2$  maps are generated with 2D regularized Laplace inversion<sup>4</sup>.

An example to construct the  $D$ - $T_2$  map of skim milk (Fig. 5d in the paper) is revealed in Fig. S6. After collecting the digitized NMR signals, the amplitudes of the echoes for different  $t_{LS}$  are evaluated (Fig. S6a). Then the echoes responses are processed with regularized Laplace inversions to generate the  $T_2$ -spectra (Fig. S6b). Finally, the  $T_2$ -spectra undergo another regularized Laplace inversions to generate the  $D$ - $T_2$  map (Fig. S6c).

## 5. Magnetic-particle-based biomolecular sensing with parallelism

Magnetic nanoparticles immersed in pure water reduce both  $T_2$  and  $T_1$  of the  $^1\text{H}$  spins of the water molecules: the former is because the magnetic nanoparticles produce the randomly fluctuating magnetic fields that accelerate the dephasing process of the  $^1\text{H}$  spins; the latter is because the magnetic nanoparticles facilitate the energy exchange between the  $^1\text{H}$  spins and the environment.

If the magnetic nanoparticles are labeled with an antibody that binds to a specific target protein and they are submerged in the water that contains the target proteins, the magnetic nanoparticles will cluster around the proteins as the labeling antibodies bind to the proteins. These magnetic nanoparticle clusters further reduce  $T_2$  of the  $^1\text{H}$  spins of the water molecules as compared to the case where the target proteins are absent and magnetic nanoparticles stay monodispersed. In contrast,  $T_1$  reduction remains more or less the same whether the magnetic nanoparticles come into clusters or stay monodispersed. So the ability to measure both relaxation times,  $T_1$  and  $T_2$ , in the control sample (without the target proteins) and in the sample under study (with the target proteins) will greatly increase our confidence in determining the presence or the absence of the target proteins. For example, if the concentrations of the magnetic nanoparticles are erroneously different between the control sample and the sample under study,  $T_1$ s of the two samples, which are supposed to be identical, will be different. By confirming that  $T_1$ s of both samples are identical, we can assure that a further reduction in  $T_2$  in the sample under study is solely due to the presence of the target proteins, not due to the different nanoparticle concentrations.

Figure S7 demonstrates this concept in our portable NMR platform with parallelism. Here we use biotin-labeled magnetic nanoparticles ( $\text{Fe}_3\text{O}_4$ , diameter: 25-30 nm) with avidin being the target protein and perform 2D  $T_1$ - $T_2$  correlation relaxometry on the samples. Figures S7a and S7b show the relationship between the relaxation times,  $T_1$  and  $T_2$ , and the concentration of the magnetic nanoparticles in the water when avidin is absent. Here we demonstrate the reduction in both  $T_1$  and  $T_2$  when the concentration of the magnetic nanoparticles is increased. Figure S7c shows a further reduction in  $T_2$  while  $T_1$  remains the same when avidin is present and the concentration of the magnetic nanoparticles is tightly controlled. This confirms that the reduction in  $T_2$  in the sample under study is indeed due to the presence of avidin in the water. Importantly, this 2D  $T_1$ - $T_2$  correlation relaxometry for magnetic particle-based biomolecular sensing, which can be used for various diagnostic applications, has been accelerated through the parallelism.

## 6. Design of the gradient coils for MRI system

The bore diameter of the magnet limits the field-of-view for the proposed MRI system. The clearance distance  $R_C$  of the frequency encoding (FE) coil, as shown in Fig. S8a, must not be larger than the radius of the bore. Since the separation between the coil ( $d_1$ ) should be  $\sqrt{3}$  times the coils' radii ( $R_1$ ), the maximum radii of the sub-coils of the Maxwell coil for a bore diameter of 26 mm is 9.8 mm. To reserve enough space for the wires, we set  $R = 9$  mm for the FE coil. The simulated  $B_0$ -gradient strength in the  $z$ -direction is 0.101 T/m at the center (Fig. S8b) and drops by 10% at 4.5 mm from the center (Fig. S8c). So we set the field-of-view of our NMR system in the  $z$ -direction as 9 mm. For phase encoding (PE), we use a Golay coil to generate a  $B_0$ -gradient in the  $x$ -direction. We set the radii of the sub-coils ( $R_2$ ) to 9.5 mm, the separations between the sub-coils (in the  $x$ -direction,  $d_2$ ) to 7.0 mm, the length between the inner and outer arcs of the sub-coils ( $L$ ) to 30 mm, and the angles subtended by the arcs ( $\theta$ ) to  $120^\circ$  (Fig. S8d). The simulated  $B_0$ -gradient strength is 0.106 T/m at the center (Fig. S8e), and also drops by 10% at 4.5 mm from the center (Fig. S8f). We also set the field-of-view of our NMR system in the  $x$ -direction as 9 mm.

## 7. Electronics for the gradient coils of the MRI system

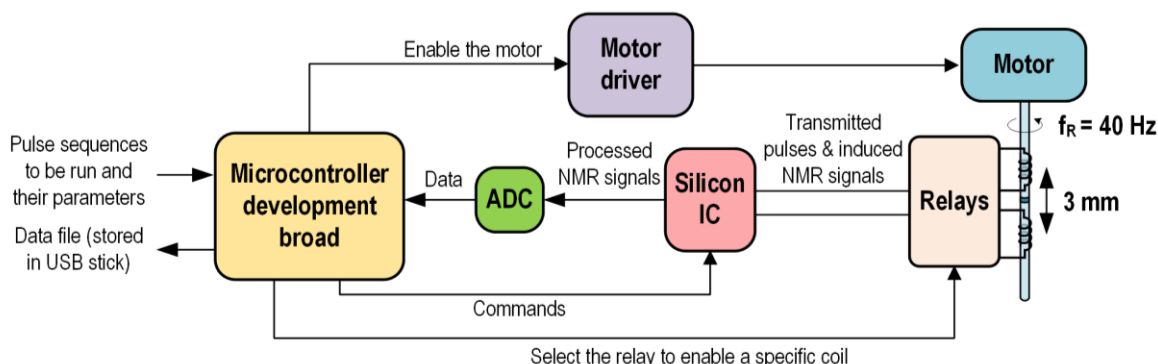
The electric currents that flow through the gradient coils of the MRI system are controlled by the electronic system. The system consists of an FPGA development board (DE2, Terasic (Hsinchu, Taiwan)), 12-bit digital-to-analog converters (DACs) (DAC7621, Texas Instruments (Dallas, Texas)), and coil drivers (Fig. S9a). Once the FPGA board receives a trigger signal from the NMR IC, it sends prearranged digital input codes to the DACs, which convert them to analog voltages. The voltages are then converted to electric currents that flow through the gradient coils by the output drivers. The coil driver has a non-inverting amplifier, which uses an operational amplifier (MAX44251, Maxim Integrated (San Jose, California)) with a resistive feedback network, followed by a unity-gain buffer, which uses another operational amplifier (OPA564, Texas Instruments (Dallas, Texas)), that can drive currents up to 1.5 A.

The relationship between the input codes generated by the FPGA and the corresponding electric currents flowing through the coil is shown in Fig. S9b. It demonstrates that the coil currents ranging from -0.3 A to 0.3 A are linearly proportional to the input codes. More specifically, in Fig. S9c, we show that the differential non-linearity (DNL) is within the  $+0.1/-0.3$  least significant bit (LSB,  $\sim 146 \mu\text{A}$ ). The rise and fall times (from 10% to 90% of the transition) of the current pulse (from 0 A to 0.3 A or vice versa) are 2.7  $\mu\text{s}$ .

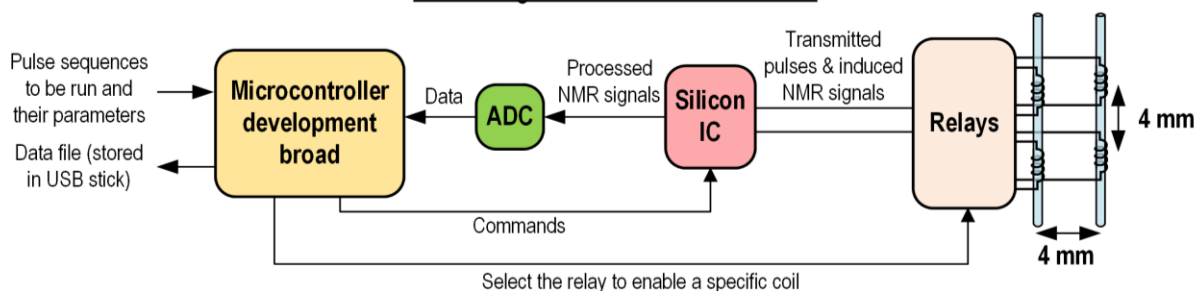
## Supplementary Figures

a

*Block diagram for NMR spectrometer*



*Block diagram for NMR relaxometer*



b

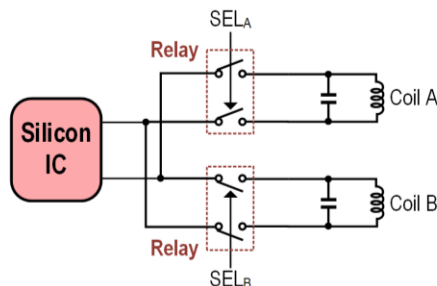


**Fig. S1. Block diagrams of the proposed NMR spectrometer and relaxometer with parallelism.**

**a.** A microcontroller translates and sends the commands to the silicon IC to initiate the NMR experiment and coordinates the relays (and the motor for spectroscopy). The NMR signals from the coil are processed by the silicon IC and the resulting signals are digitized by the analog-to-digital converter. The digitized data are captured by the microcontroller. Finally, the data are stored on a USB stick for further processing in a computer. The microcontroller governs the overall timing of the spectrometer and relaxometer for automated and time-interleaved NMR scans. The motor and motor driver are operated by the microcontroller to rotate the tube (samples) during spectroscopy measurements to improve the resolution of the NMR signals. **b.** The  $N$  coils ( $N = 2$  in this example illustration) are connected to the silicon chip via mechanical relays G6K-2F-RF from Omron Electronics (Kyoto, Japan). The relays are controlled by the selection signals  $SEL_A/SEL_B$  from the microcontroller. Mechanical relays do not add appreciable thermal noise.

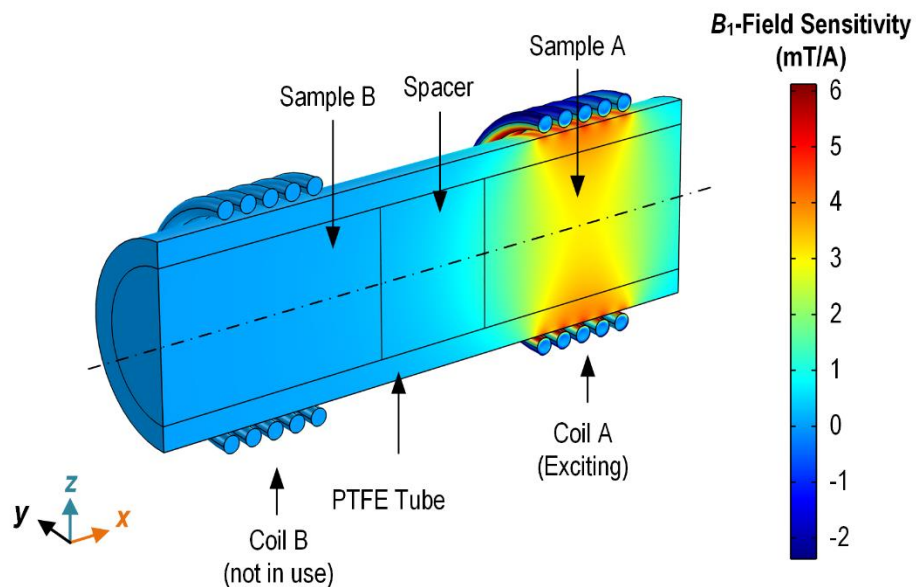


**Fig. S2. Simulated magnetic-field pattern of the NMR coil.**

When the two tube-sharing coils are separated by 3 mm (center-to-center pitch), the RF magnetic field generated by the exciting coil (coil A) is reduced by at least 10 times across the entire sample surrounded by the unexcited coil (coil B).

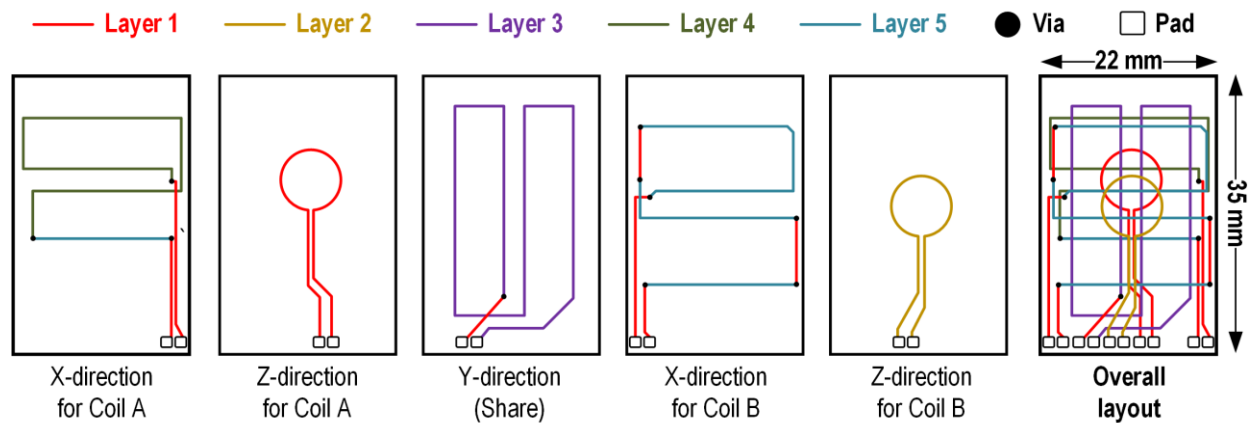


**Fig. S3. The layout of the shim coils fabricated on PCB for 2 NMR samples.**

Each sample has individual shim coils to correct the  $B_0$ -gradients in the  $x$ - and  $z$ -directions and shares the same shim coil in the  $y$ -direction. Five layers of conductors (0.3 mm width) comprise the shim coils. Two 1.6 mm thick identical PCBs are placed face-to-face (on top and bottom of the samples) inside the magnet.

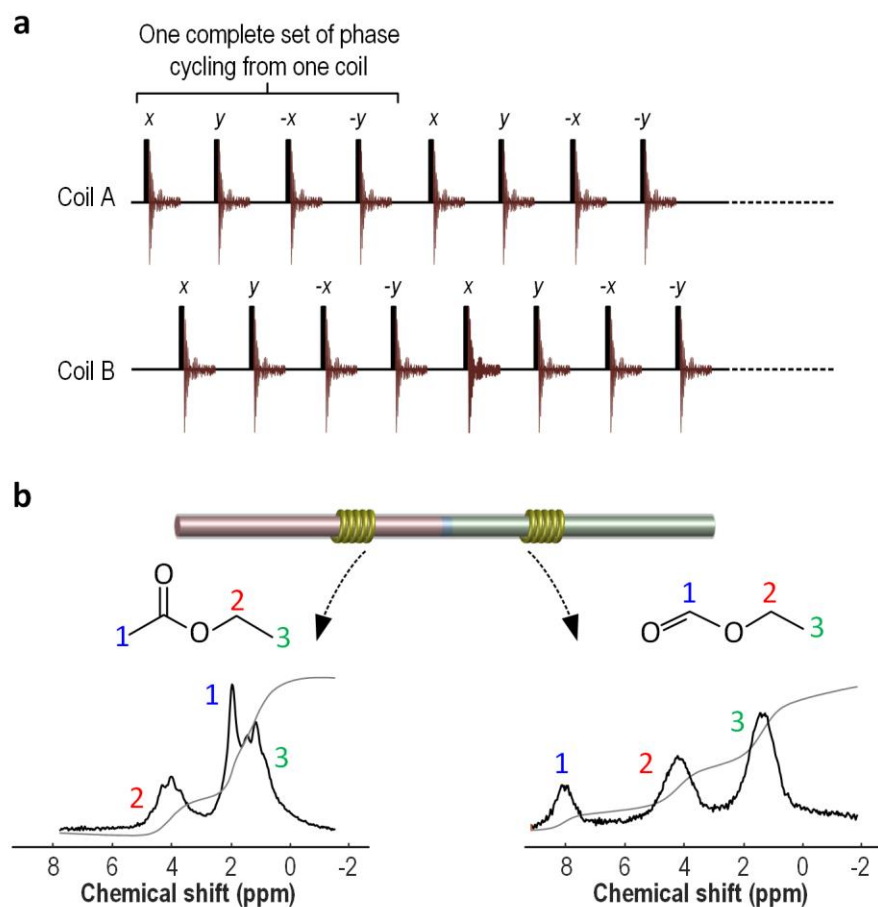


**Fig. S4. Time-interleaved 1D  $^1\text{H}$  NMR spectroscopic experiment.**

**a.**  $^1\text{H}$  FID pulse sequences for two coils in time-interleaved fashion. The letters above each individual sequence denote the phase of the transmitter where the phase of the receiver is fixed. Four-step phase cycling is applied to cancel the imbalance between the receiver's quadrature channels. Each coil runs identical pulse sequences, and the collected results from them are processed with the  $B_0$ -calibration algorithm. The calibrated results are then analyzed (for distinct samples) or combined (for identical sample) to improve the SNR. **b.** Measured 1D  $^1\text{H}$  spectra of 2 samples of different contents (ethyl acetate and ethyl formate) without motional averaging. Although the chemical shifts of the samples are resolved, the  $J$ -coupling, which contains information about the connectivity of the chemical structure, cannot be distinguished due to the poor field inhomogeneity  $\Delta B_0/B_0$ .

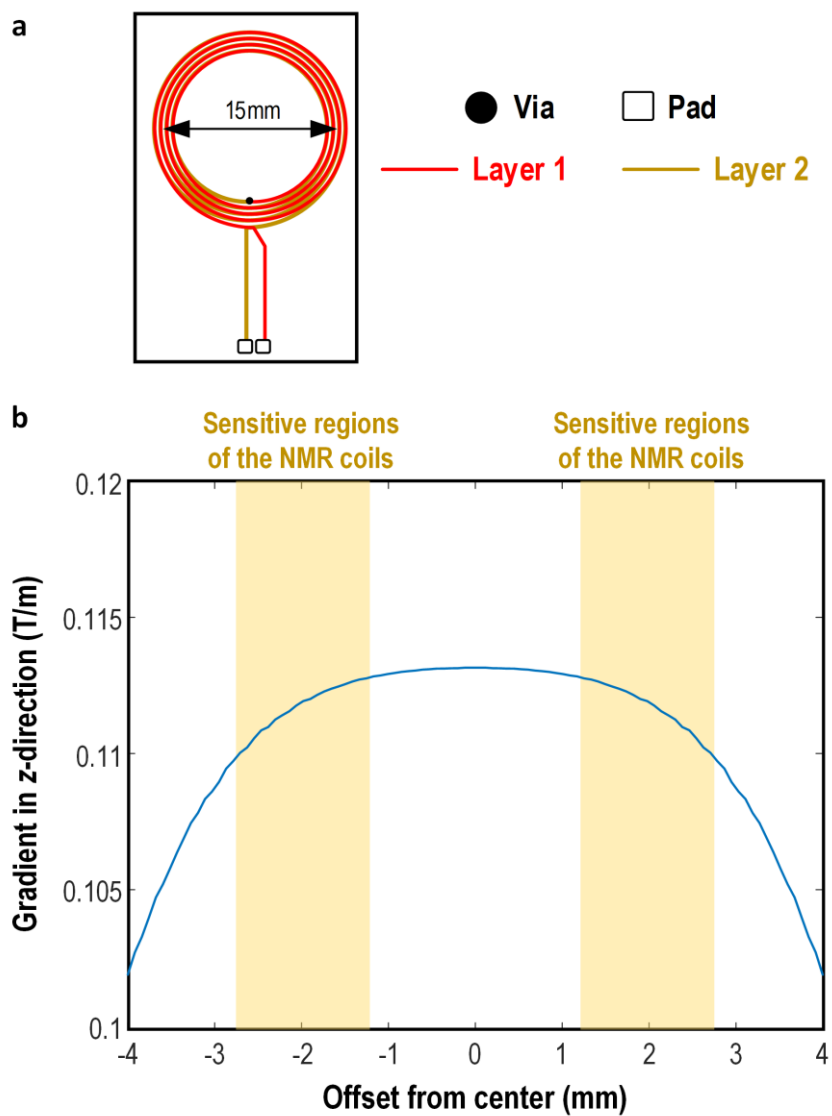


**Fig. S5. The gradient-coil for relaxometry.**

**a.** The PCB layout of the gradient coil for relaxometry. Like the shim coils, two identical units are placed inside the magnet, sandwiching the samples at the top and bottom. **b.** Simulated  $B_0$ -gradient of the gradient coils in the  $z$ -direction versus the distance from the center of the gradient coil. The simulated difference in the  $B_0$ -gradient is around 3% across the coil.

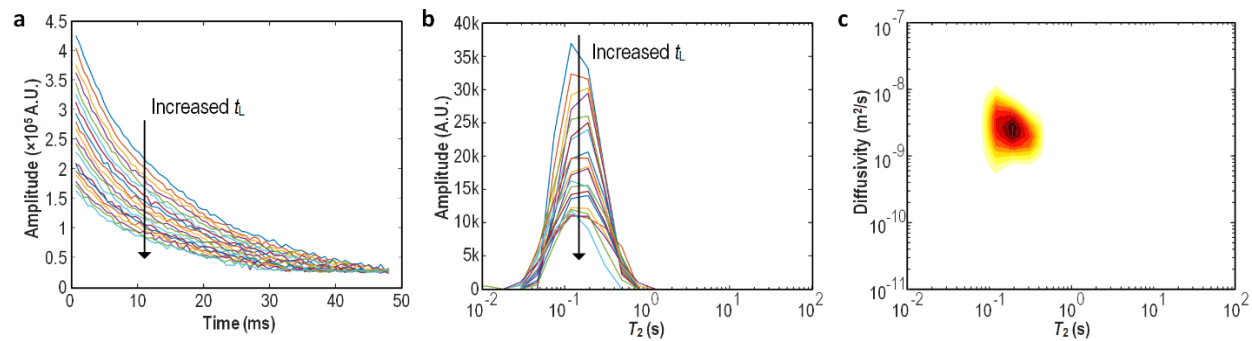


**Fig. S6. Measured diffusion-edited NMR relaxation data of skim milk.**

**a.** Echo signals from the skim milk with 20 different  $t_L$  values (from 1 ms to 6.7 ms). The amplitude of the echo signals decreases with an increasing  $t_L$ . **b.** Regularized Laplace inversions are applied to the echo signals to obtain the  $T_2$ -spectra. Whereas the  $T_2$ -spectra exhibit different amplitudes with the differing  $t_L$  values, they feature similar  $T_2$ -distributions. **c.** The  $D$ - $T_2$  map of the skim milk (identical to Fig. 5d in the article) is obtained by taking another regularized Laplace inversion on the  $T_2$ -spectra of Part (b).

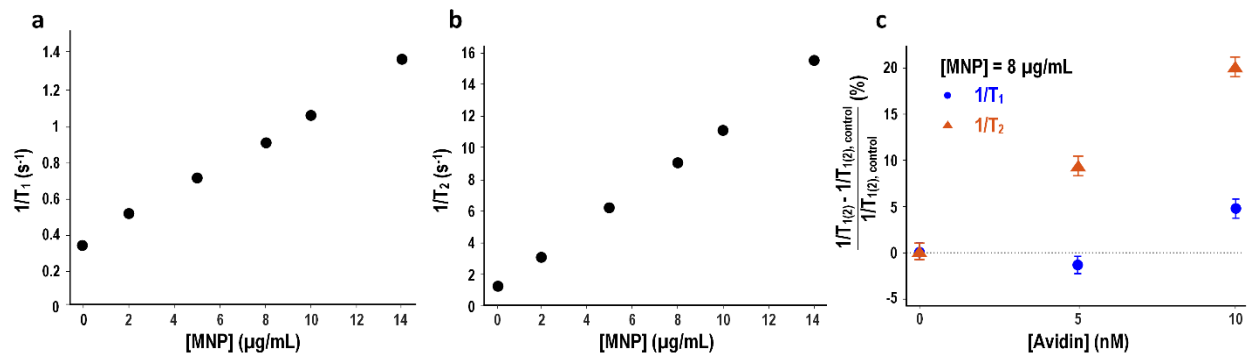


**Fig. S7. Relaxation rates measurement from avidin samples with the NMR relaxometer.**

**a-b.** Spin-lattice and spin-spin relaxation rates ( $1/T_1$  and  $1/T_2$ ) in <sup>1</sup>H NMR with varying concentration of biotinylated magnetic nanoparticles in water in the absence of avidin. **c.** Changes in  $1/T_1$  and  $1/T_2$  in <sup>1</sup>H NMR of water with varying concentration of avidin in water while the concentration of biotinylated magnetic nanoparticles is fixed to 8 μg/mL.

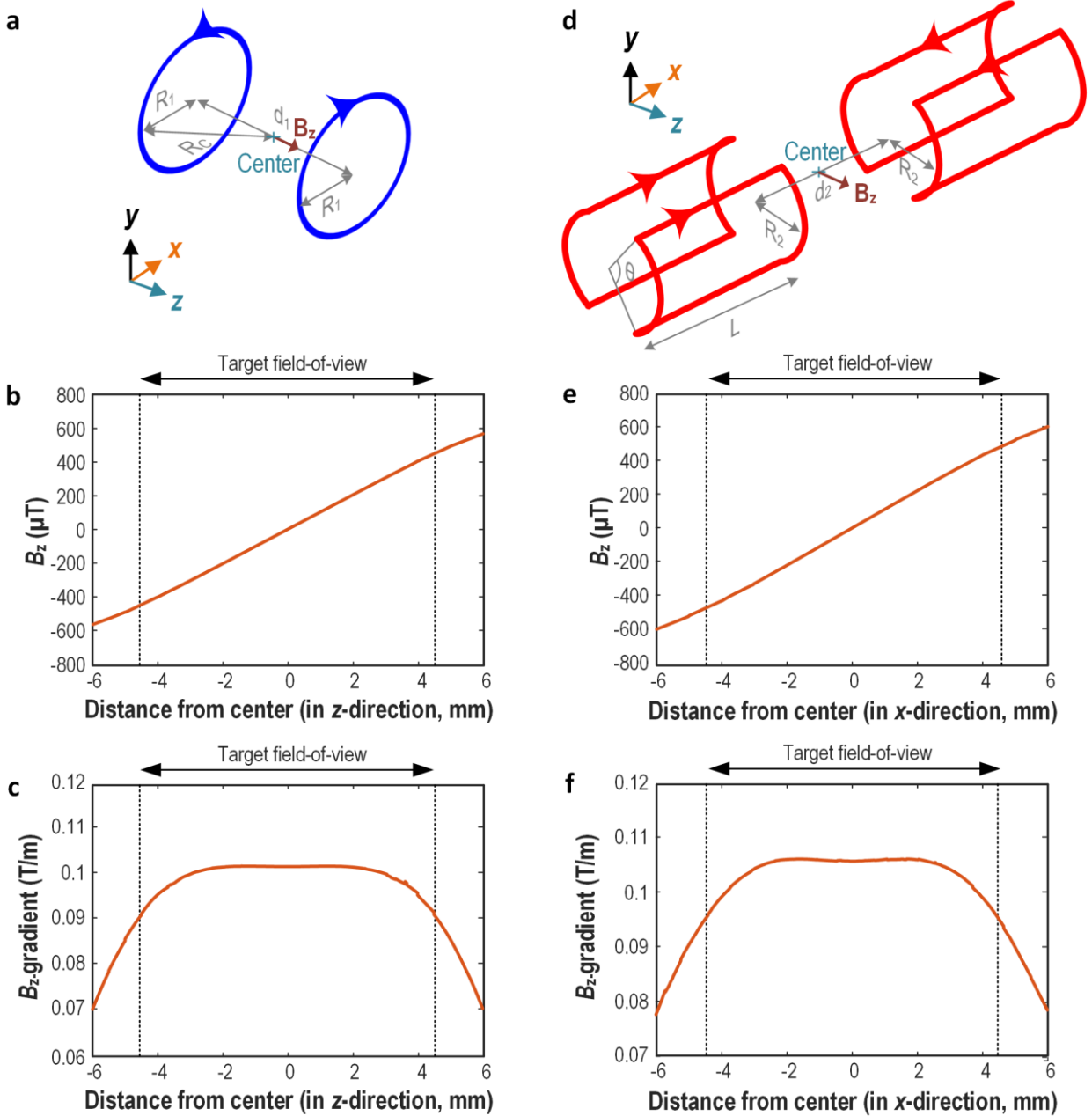


**Fig. S8. Design and simulation of the MRI gradient-coils.**

**a.** The gradient coil of the Maxwell geometry to generate  $G_f$ . Each of the two circular sub-coils has 8 turns and carries current in the opposite direction with each other. The magnetic field generated by the coil in the  $z$ -direction  $B_z$  varies linearly with  $z$  and enables FE for the MRI system. **b&c.** The simulated  $B_z$  and  $B_z$ -gradient in COMSOL with a current of 1 A ( $R_1 = 9.0$  mm,  $d_1 = 15.6$  mm). The  $B_z$ -gradient stays within 10% from the center point across the field-of-view. **d.** The gradient coil of the Golay geometry to generate the  $G_p$ . Each of the four sub-coils has 8 turns.  $B_z$  changes linearly in the  $x$ -direction, enabling PE for the MRI system. **e&f.** The simulated  $B_z$  and  $B_z$ -gradient in COMSOL with a current of 1 A ( $R_2 = 9.5$  mm,  $d_2 = 7.0$  mm,  $L = 30$  mm,  $\theta = 120^\circ$ ). The  $B_z$ -gradient stays within 10% from the center point across the field-of-view.

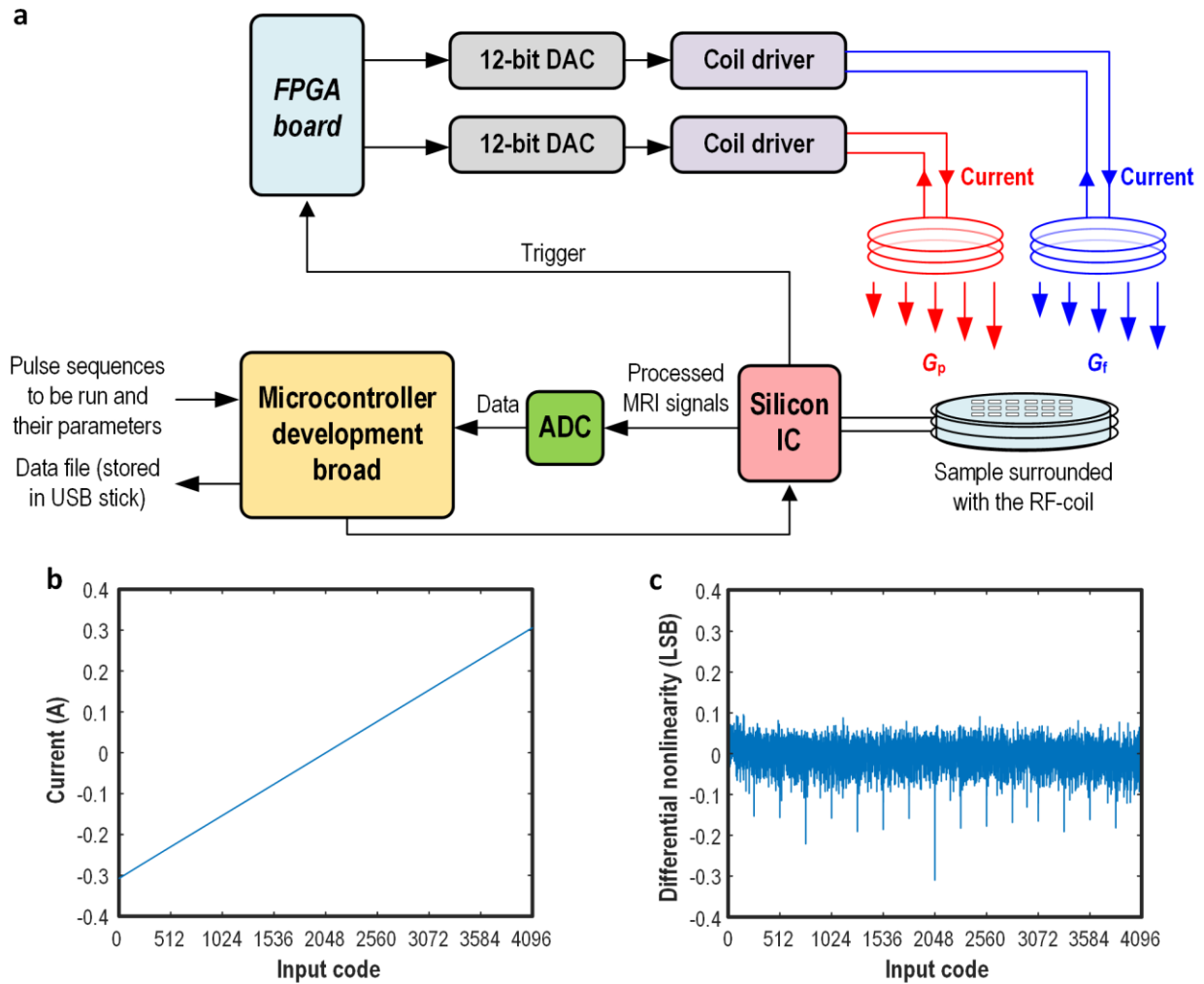


**Fig. S9. The hardware for the portable MRI.**

**a.** The block diagram of the proposed MRI system. A trigger signal from the NMR IC is used to synchronize the FPGA development board with the NMR IC. When triggered, the FPGA board outputs digital codes that are converted by the DACs and coil drivers to the electric currents flowing through the corresponding gradient coils to generate the  $B_0$ -gradients. **b.** The output currents flowing through the gradient coils Vs. the input codes generated by the FPGA. **c.** Differential nonlinearity (in term of the least significant bit of the input code) of the currents flowing through the gradient coils.

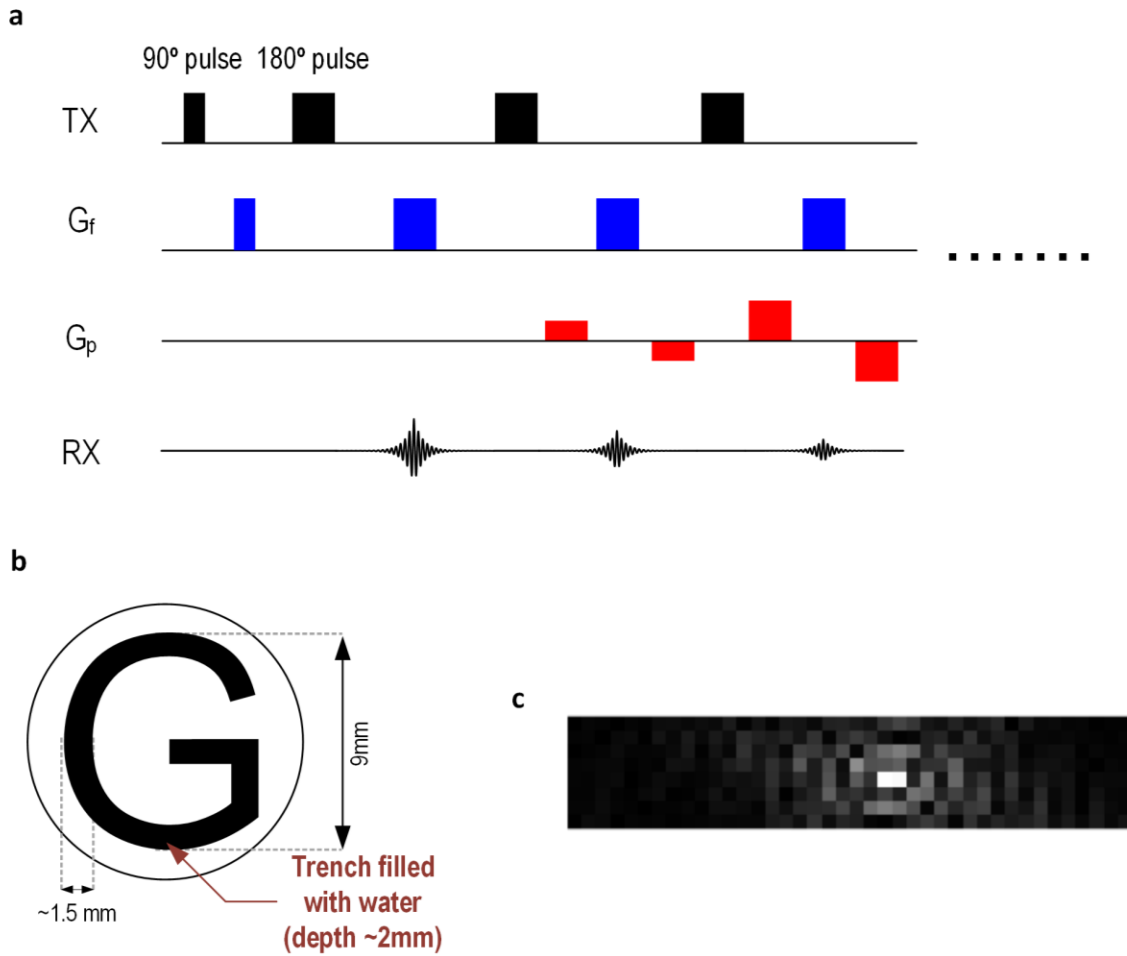


**Fig. S10. The MRI experiment on the phantom.**

**a.** A turbo spin echo sequence for the MRI experiment. The initial 90°-pulse is followed by multiple 180°-pulses to acquire a sequence of images with each scan. Note a dephasing lobe for  $G_f$  is presented between the 90°-pulse and 180°-pulse to cause the spins to rephase at the center of the subsequent echoes.

**b.** The phantom used to illustrate the functionality of the MRI system. A letter 'G' is engraved on the acrylic substrate by the laser printer. Then the trench (depth: 2 mm) is filled with deionized water.

**c.** The  $k$ -space of the image. It has 8 PE steps and each step contains 40 digitized data points. We fill the lower half of the  $k$ -space by mirroring the data from the upper half to reduce the image acquisition time, thanks to the conjugate symmetry of the  $k$ -space.

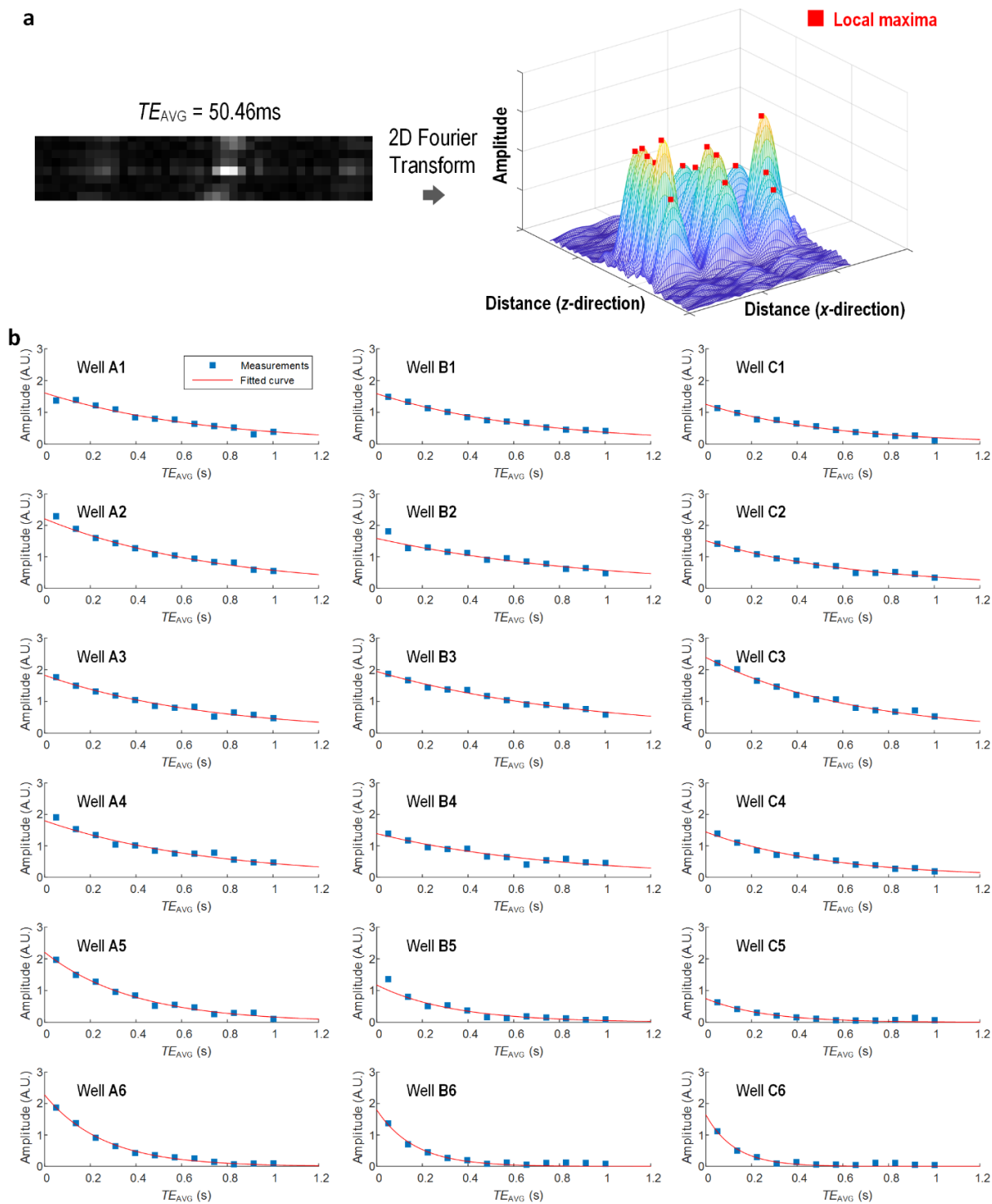


**Fig. S11. Original data for the high-throughput  $T_2$ -screening with MRI.**

**a.** Collected  $k$ -space data of the MRI image for the  $6 \times 3$  wells measurement with  $TE_{AVG}$  of 50.46 ms. Then 2D Fourier Transform is applied to the data to acquire the image. The intensities of the signals from the wells are evaluated from the local maxima of the images. **b.** The intensities of the signals (blue square) from the samples on the acquired images for the MRI experiments (*i.e.*, from Fig. 6) against  $TE_{AVG}$ . The data are fitted to a mono-exponential decay curve (red line) to estimate the corresponding  $T_2$  of the sample.

## References:

1. Takasumi, K.; Dent, P.; Liu, J.; Marinescu, M.; Walmer, M., New grade of temperature compensated samarium cobalt permanent magnets and design considerations. *IEEE Int. Vacuum Electron. Conf.* **2009**, 565-566.
2. Ha, D.; Paulsen, J.; Sun, N.; Song, Y. Q.; Ham, D., Scalable NMR spectroscopy with semiconductor chips. *Proc. Natl. Acad. Sci. U. S. A.* **2014**, *111* (33), 11955-11960.
3. Gunther, H., *NMR spectroscopy: basic principles, concepts, and applications in chemistry*. Wiley: **1995**.
4. Marino, L. G., Regularized inverse Laplace transform. **2007**, <https://www.mathworks.com/matlabcentral/fileexchange/6523-rilt>